Materials Today • Volume xxx, Number xx • xxxx 2018

ELSEVIER

Ternary interfacial superstructure enabling extraordinary hydrogen evolution electrocatalysis

Hongliang Jiang [1,†], Yunxiang Lin [1,†], Bingxu Chen [2,†], Youkui Zhang [1], Hengjie Liu [1], Xuezhi Duan [2,*], De Chen [3], Li Song [1,*]

[1] National Synchrotron Radiation Laboratory, CAS Center for Excellence in Nanoscience, University of Science and Technology of China, Hefei, Anhui 230029, China
[2] State Key Laboratory of Chemical Engineering, East China University of Science and Technology, 130 Meilong Road, Shanghai 200237, China
[3] Department of Chemical Engineering, Norwegian University of Science and Technology, N-7491 Trondheim, Norway

Realizing large-scale electrochemical hydrogen evolution in alkaline and neutral media by robust and non-noble-metal heterogeneous catalysts is highly ambitious due to the sluggish reaction kinetics at low H^+ conditions. Herein, highly efficient hydrogen evolution reaction (HER) catalysts, comprising Ni, NiO clusters, and defective carbon, are successfully constructed via a facile and large-scale route. Multiple synchrotron radiation-based X-ray spectroscopic characterizations, combining high-resolution transmission electron microscopy measurements, indicate the formation of ternary interfacial superstructure with intimate interfacial coupling through abundant Ni—O—C bonds. Impressively, the optimized catalyst loaded onto the usual glass carbon electrode exhibits exceptional catalytic activities with overpotentials of 64 and 76 mV to reach 10 mA cm^{-2} in 1 M KOH and 1 M phosphate buffer solution (PBS), respectively, representing one of the best non-noble-metal HER electrocatalysts to date. Insights into the metal/oxide interfacial effects through density functional theory calculations reveal that the interface sites could efficiently lower the energy barrier of the rate-determining step (RDS), contributing to the fast reaction kinetics. This work not only provides comprehensive insights into interfacial feature of highly active HER catalysts but also broadens the fundamental understanding of interfacial effects toward HER catalysis.

Introduction

Hydrogen evolution by water electrolysis is generally considered as a very promising way to realize large-scale hydrogen production [1–4]. It holds the key to developing highly efficient and cost-effective catalysts as alternatives to high-cost Pt group materials [5,6]. Although some non-Pt catalysts show comparable and even surpassing catalytic performance with respect to Pt-based catalysts in acidic conditions [7–9], the development of non-Pt catalysts with satisfactory catalytic performance in alkaline and neutral media for alkaline water and sea-water electrolysis is still a challenge [10–17]. For hydrogen evolution reaction (HER) in alkaline and neutral media, the so-called Volmer step, the water dissociation, is identified as the rate-determining step (RDS) [18–22]. However, its high-energy barrier leads to the sluggish reaction kinetics and hinders the overall HER process [23]. In this regard, the researchers have developed various highly active HER catalysts [24–27]. In particular, the binary metal/oxide interfacial structures compared to the single-phase ones exhibit synergistic effects on the water dissociation and thus remarkably enhance HER catalytic performance [28–31]. Compared to other catalysts [32–34], nickel-based materials generally exhibit unique HER performance with low overpotential and gain extensive attention due to earth-abundant reserves and unique eight electrons in the 3d electron orbital that contributes to facile structural

* Corresponding authors.
E-mail addresses: Duan, X. (xzduan@ecust.edu.cn), Song, L. (song2012@ustc.edu.cn).
† H. Jiang, Y. Lin and B. Chen contributed equally.

https://doi.org/10.1016/j.mattod.2018.01.033

Please cite this article in press as: H. Jiang et al., (2018), https://doi.org/10.1016/j.mattod.2018.01.033

regulation [13]. Moreover, carbon supports are generally employed as electronic conductor [10,29]. Nevertheless, the efficient integration of the metal/oxide/carbon components and the investigation of the interaction of these components are rare. Therefore, developing synthesis strategies with precise structure designs are highly desirable but challenging to fabricate highly efficient ternary HER catalysts, i.e., metal/oxide/carbon interfacial structures. Furthermore, probing the ternary interfacial interactions is of great significance to unravel the catalytic mechanisms and enhance the catalytic performance.

On the other hand, material-characterization methods with the atomic level precision are crucial to obtain an in-depth understanding of the above-mentioned interfacial structure and effects by combining multiple characterization techniques and theoretical calculations [35–39]. However, the complexity of the metal–oxide–carbon ternary structure impedes exhaustive structure identification. Currently, synchrotron radiation-based X-ray absorption spectroscopy (XAS) techniques gain popularity due to the unique advantages in analyzing atomic and electronic structures [40–44]. For instances, the soft XAS is highly effective to analyze the interfacial interaction between the carbon supports and metal/oxide species [44]. The hard XAS, X-ray absorption fine structure (XAFS) and the extended X-ray absorption fine structure (EXAFS), can precisely analyze the atomic coordination structure and coordination number of the metals and oxides [45]. Thus, the combination of the soft and hard XAS would obtain distinctive superiorities in facilitating the understanding of the metal–oxide–carbon interfacial structure.

In the present work, unique ternary interfacial structures were elaborately obtained by thermal treatments of simple coordination compounds. The as-prepared materials consisted of ultrasmall Ni nanoparticles, mounted NiO clusters, and defective ultrathin carbon layers (marked as Ni/NiO@C), forming 'pomegranate'-like nano-superstructure. More particularly, accessible ternary interfacial nanostructure with intimate interfacial contact was formed among the three components, as revealed by material-characterization methods with the atomic level precision, especially the soft and hard XAS measurements. The catalytic performance of the ternary interfacial structure materials as the HER electrocatalysts was evaluated by systematic electrochemical tests. Furthermore, density functional theory (DFT) calculations were performed to understand the Ni/NiO interfacial effects on the overall HER process.

Results and discussion

Synthesis of ternary interfacial superstructure

The precursor, ethylenediaminetetraacetic acid nickelous salt (EDTA–Ni, Figure S1), was readily prepared by the coordination process of Ni^{2+} and EDTA acid (see the Materials and Methods for details). The analysis (Figure S2) toward element compositions of the EDTA–Ni indicates that the valence state of Ni element is determined to be mainly +2, with the content of 19.2 wt%. Then, direct thermal treatments of EDTA–Ni at the designed temperature (400 and 500 °C) were performed to obtain the target Ni—C-based structure through the reduction process of Ni^{2+} and organic ligands in inert atmosphere, as schematically illustrated in Figure 1. Finally, on account of the instability of

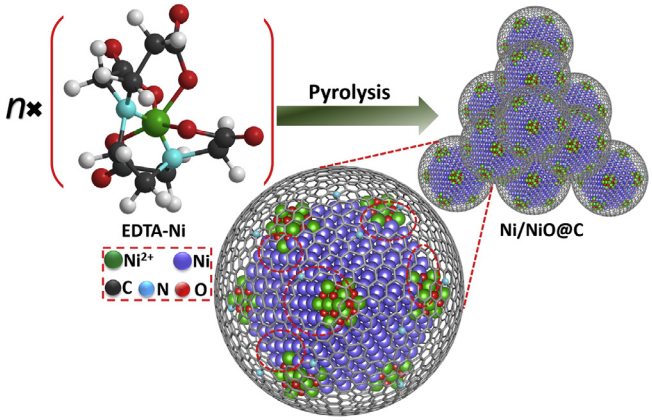

FIGURE 1

Schematic illustration for the formation process of Ni/NiO@C. The direct annealing reduction in inert atmosphere was employed with ethylenediaminetetraacetic acid nickelous salt (EDTA–Ni) as precursors. The red dotted circles illustrate carbon defect sites.

ultrasmall transition metal nanoparticles in the air, the two annealed fresh samples were placed in the air for one month, then the relatively stable ternary structures (denoted as Ni/NiO@C-1 and Ni/NiO@C-2 which are from the 400 and 500 °C-annealed fresh samples, respectively) were obtained. For full consideration, the control sample (denoted as Ni/NiO@C-3) was also prepared by placing the 500 °C-annealed fresh sample in the inert atmosphere at room temperature.

Chemical compositions and microstructures of ternary interfacial superstructure

Typically, the powder X-ray diffraction (PXRD) and electron microscopy were conducted to investigate the compositions, as summarized in Figure 2. From Figure 2a, the XRD patterns of the Ni/NiO@C-2 and Ni/NiO@-3 could be indexed to the characteristic diffraction peaks of the cubic Ni (JCPDF 65-0380). Note that for the 400 °Cannealing obtained Ni/NiO@C-1, besides the diffraction peaks from the Ni, the NiO component could also be found probably due to inadequate reduction in Ni^{2+} at relatively low annealing temperature. The transmission electron microscopy (TEM) images of the three Ni/NiO@C (Figures S3, 2b, and c) suggest that these nanoparticles with the size of about 5 nm were well embedded in graphene cages. Meanwhile, these Ni-contained graphene cages were covalently connected, forming typical 'pomegranate'-like nano-superstructure. Furthermore, the Ni/NiO@C-2 as a representative, high-resolution TEM (HRTEM) was performed (Figures 2d, S4, and S5). As shown in Figure 2d, the lattice fringe distances of 2.04, 1.78, 2.11 and 3.41 Å coincide well with the Ni(111), Ni(200), NiO(200) and C(002) facets, respectively. This result is further confirmed by selected area electron diffraction (SAED) pattern (inset of Figure 2d). One could see that, besides the binary interfacial structures of Ni nanoparticles and carbon layers, ternary interfacial structures could also be observed among Ni, NiO, and carbon layers, which are further verified in Figure S4. Specially, NiO nanoparticles (about 5 nm) without coated carbon layers also existed at the outside edge of materials (Figure S5). From the above TEM analysis, it can be inferred that the formation of the NiO composition in the Ni/NiO@C-2 was probably ascribed

Please cite this article in press as: H. Jiang et al., (2018), https://doi.org/10.1016/j.mattod.2018.01.033

to the oxidation of metal Ni in air such that the Ni/NiO interfacial structure mainly existed at the carbon defect sites. Meanwhile, the existing carbon layers could protect the Ni nanoparticles from excessive oxidation; thus, the stable ternary interfacial structure was formed. In order to further probe the chemical compositions and their distributions, the energy dispersive X-ray (EDX) mapping of the Ni/NiO@C-2 was presented (Figure 2e), which indicates the uniform distribution of Ni, C, O, and N elements. N elements derived from N-contained organic ligands of EDTA. Notably, the uniform presence of O elements into overall superstructure suggested that the NiO component was not just at the outside edge of materials. The NiO probably exists on each Ni-contained graphene cage such that abundant ternary Ni—NiO—C interfaces are formed, as illustrated in Figure 1. In order to verify the feature of carbon layers, the control sample without the NiO component (marked as Ni/NiO@C-2 acid treatment) was also prepared through the acid treatment of the Ni/NiO@C-2 in room temperature (see the Materials and Methods for details). From thermogravimetry analysis (TGA) results (Figure S6) of the Ni/NiO@C-2 and Ni/NiO@C-2 acid treatment, we can conclude that the Ni species in the Ni/NiO@C-2 with the Ni content of 55.0 wt% could be efficiently removed through acid leaching, suggesting the accessibility of most of carbon layers. Such accessibility of carbon layers also contributes to the formation of the above unique ternary interfacial structure due to the entering of oxygen from carbon defect sites. Next, it holds the key to further exploring the interfacial properties and effects, as discussed in the following sections.

Investigation of interfacial properties

In order to achieve the precise characterization of ternary interface properties, synchrotron radiation-based spectroscopy technologies, including synchrotron radiation X-ray photoelectron spectroscopy (SRXPS) and the XAS, were introduced. First, surface-sensitive spectroscopic techniques, XPS, and soft X-ray absorption near edge structures (XANES) measurements were employed to explore the local structure (Figure 3). As shown in Figure 3a, the dominant feature A assigned to metallic Ni in the high-resolution Ni 2p XPS spectrum suggests that the NiO compositions are not detected probably due to the extremely low content in the Ni/NiO@C-2 and Ni/NiO@C-3 [46]. However, for the Ni/NiO@C-1, another feature B assigned to Ni^{2+} could be

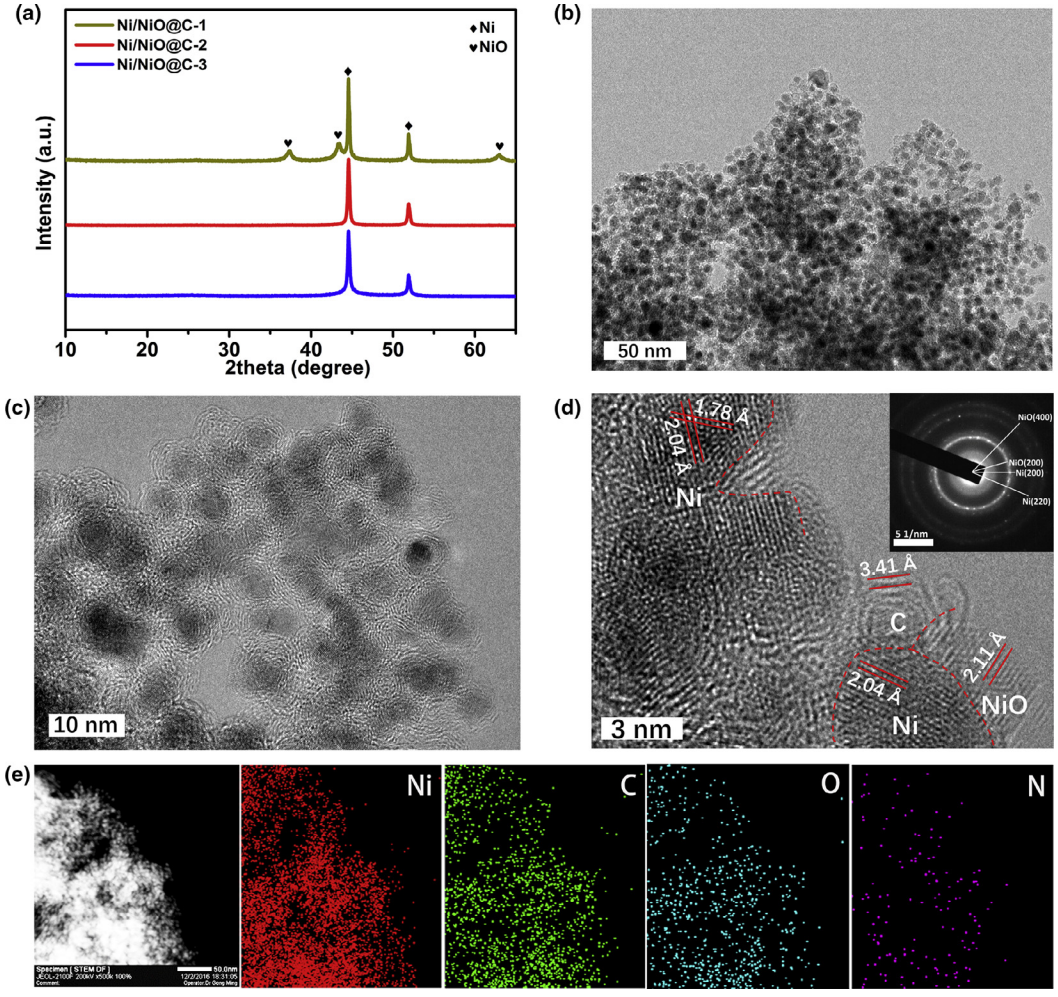

FIGURE 2

Chemical compositions and microstructure of ternary interfacial superstructure of Ni/NiO@C. (a) PXRD patterns of the three Ni/NiO@C. (b and c) TEM images of the Ni/NiO@C-2. (d) HRTEM image (Inset: the SAED image) and (e) STEM EDX mappings of the Ni/NiO@C-2.

Please cite this article in press as: H. Jiang et al., (2018), https://doi.org/10.1016/j.mattod.2018.01.033

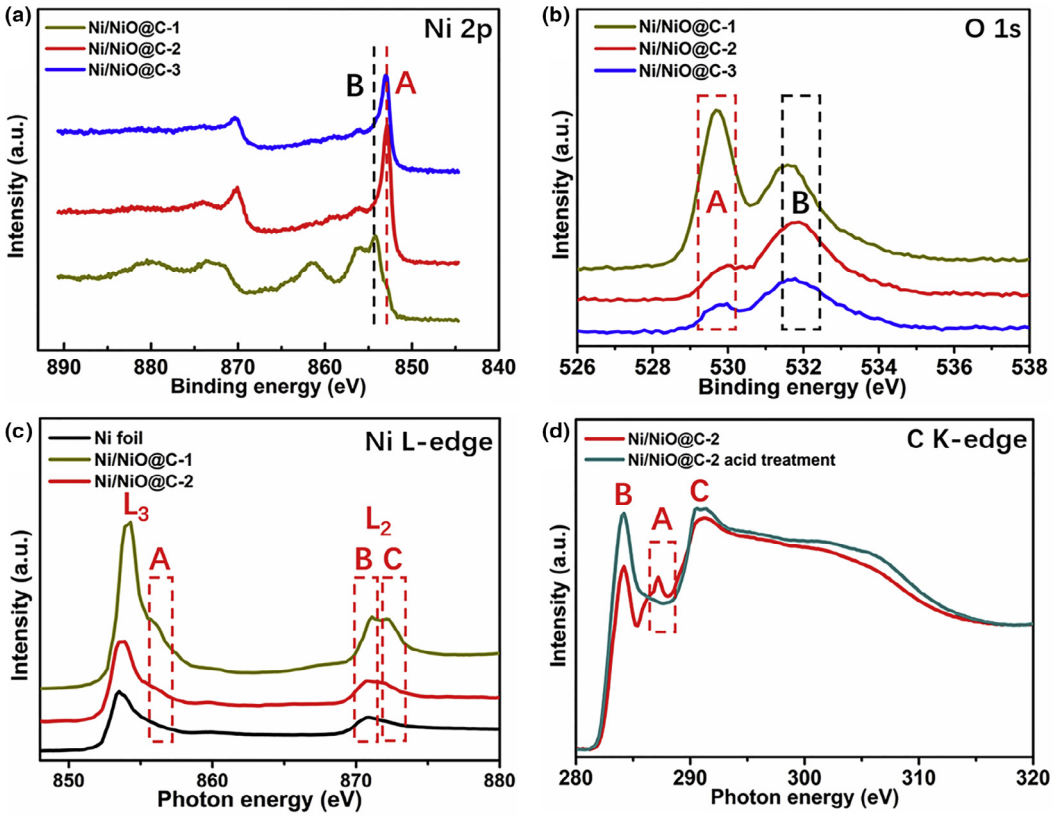

FIGURE 3

Interfacial identifications of ternary interfacial superstructure of Ni/NiO@C. (a) Ni 2p XPS spectra of the three Ni/NiO@C. (b) O 1s XPS spectra of the three Ni/NiO@C (c) XAS spectra of Ni foil, Ni/NiO@C-1 and Ni/NiO@C-2 at Ni L-edge. (d) XAS spectra of Ni/NiO@C-2 and Ni/NiO@C-2 acid treatment at C K-edge.

also observed due to the relatively high NiO content, in accordance with the previous XRD analysis. Furthermore, the high-resolution O 1s XPS spectra (Figure 3b) clearly show two main peaks that were recognized as O species of the NiO compositions (feature A) and the absorbed O species from air (feature B), verifying the co-existence of Ni and NiO [47,48]. Additionally, the peak area of the characteristic peak (feature A) implies that the NiO content followed the sequence: Ni/NiO@C-1 > Ni/NiO@C-2 > Ni/NiO@C-3. The high-resolution C 1s and N 1s XPS spectra reveal the N-doping in the defective carbon layer (Figure S7). To further shed light on the chemical environments of Ni sites, the soft XANES spectra at Ni $L_{2,3}$ edges were recorded. As shown in Figure 3c, compared to the Ni foil, the shoulder peak A at the high-energy side of the L_3 peak and splitting of the L_2 peak are assigned to those of the $L_{2,3}$ edge spectrum, further corroborating the interface structure of Ni and NiO [49]. Then, the next question is how the interface of carbon layers and Ni species interact. From the C K-edge XAS spectrum in Figure 3d, three main peaks located at 287.2 eV, 284.2 eV, and 291.3 eV are observed and marked as A, B, C, respectively. Feature B and feature C are typically assigned to the π^* states and σ^* states of the carbon ring structure [50]. And, feature A is assigned to the interfacial interaction between Ni species and carbon layers [51]. Meanwhile, the feature A also indicates the defective feature of carbon layer, which is further demonstrated by the D and G bands in the Raman spectrum (Figure S8). In our control experiments, the feature A completely disappeared for the case of Ni/NiO@-C-2 after acid treatment, which revealed that the feature A mainly ascribed to the Ni—O—C bonds and meanwhile verified the accessibility of carbon layers in the Ni/NiO@-C-2. Besides, compared to that of the Ni/NiO@-C-2 acid treatment, the significantly decreased features B and C of the Ni/NiO@-C-2 also confirm the interfacial electron transfer from the Ni species to carbon layers due to strong interfacial interaction, further revealing the formation of the ternary Ni—NiO—C interfaces with high-density level [52]. These interface investigation results strongly verify the formation of ternary interfacial structures with intimate interfacial contact and high-density level.

To further identify the coordination structure of Ni species in samples, XAFS measurements were conducted. As exhibited in Figure 4a, obvious differences in intensity and position of the characteristic peak for three Ni/NiO@C could be observed in reference to the standard Ni foil and NiO foil, implying different chemical environments of Ni species in these Ni/NiO@C samples. Moreover, the absorption threshold of the Ni/NiO@C-2 is close to that of the Ni foil and also positively shifted (the inset of Figure 4a), further suggesting that the Ni/NiO@C-2 typically consisted of dominated metal Ni with tiny oxides [53]. With respect to the relative amount of the NiO composition in the Ni/NiO@C samples, the above XRD and XPS are unable to achieve the request due to very low NiO content. On account of high penetrability of XAFS measurements in transmission mode, the content ratios of Ni and NiO were estimated by linear

Please cite this article in press as: H. Jiang et al., (2018), https://doi.org/10.1016/j.mattod.2018.01.033

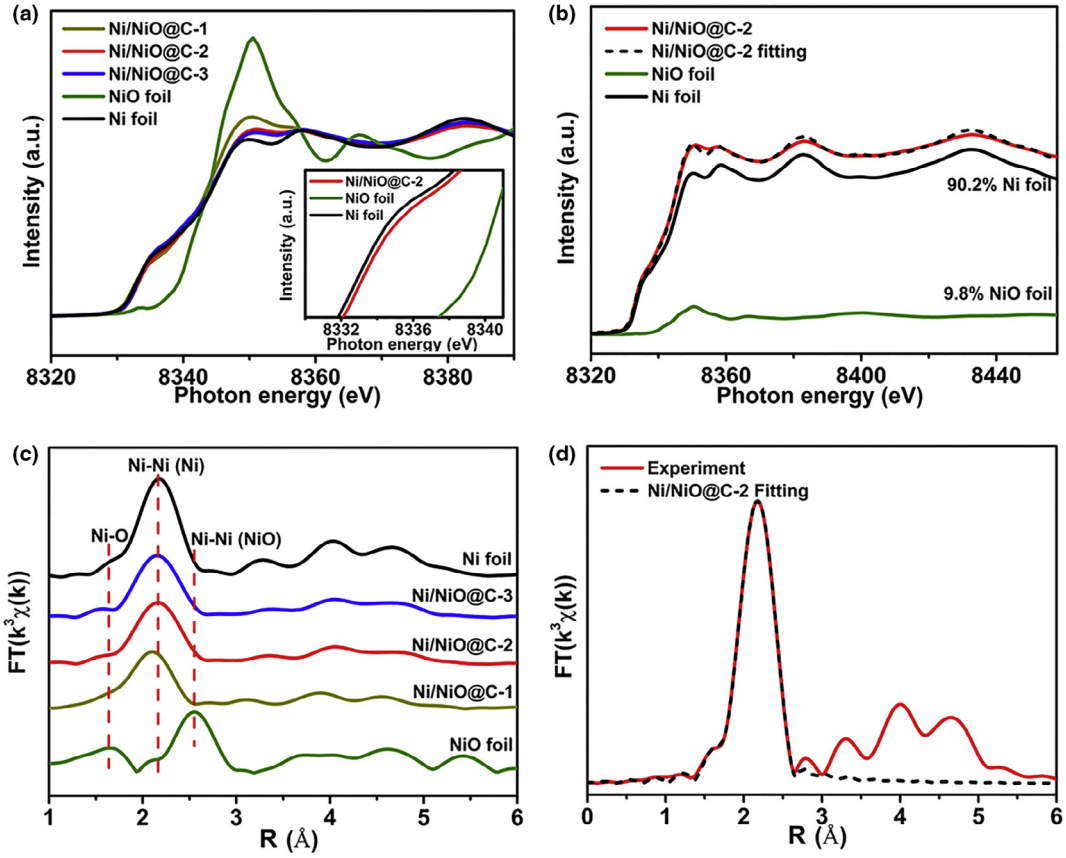

FIGURE 4

XANES and EXAFS spectra of ternary interfacial superstructure of Ni/NiO@C. (a) Normalized Ni K-edge XANES spectra of the three Ni/NiO@C as well as the Ni foil and NiO foil reference samples. (b) Linear combination fitting spectra of the Ni/NiO@C-2 based the spectra of the measured Ni/NiO@C-2, the Ni foil, and the NiO foil. (c) The corresponding k^3-weighted χ(k)-function of the Ni K-edge EXAFS spectra. (d) EXAFS fitting curves of the Ni/NiO@C-2.

combination fitting of Ni foil and NiO foil standard patterns [46] (Figures 4b, S9, and S10). As summarized in Table S1, the NiO content is 21.3 wt% for the Ni/NiO@-C-1, 9.8 wt% for the Ni/NiO@-C-2, 5.2 wt% for the Ni/NiO@-C-3, respectively, which is consistent with the above O 1s XPS results. The EXAFS and fitting curve results (Figures 4c and d, S11) are obtained to extract bond lengths and coordination numbers (CNs). In reference to the standard NiO foil and Ni foil, the significantly decreased CN for Ni—O bonds and slightly decreased CN for Ni—Ni bonds in the three Ni/NiO@C-2 samples further confirm that the NiO clusters were mounted on the dominated metal Ni (Table S2).

HER performance evaluation in alkaline and neutral media

Developing efficient HER electrocatalysts operated in alkaline and neutral media is of great importance for alkaline water electrolysis, microbial and sea-water electrolysis [31]. Here, the HER catalytic performance of these Ni/NiO@C was evaluated in a standard test system (see the Materials and Methods for details). For better comparison, the control sample with 79.9 wt% NiO content (Figures S12–S14) was also obtained through oxidizing Ni/NiO@C-2 (marked as Ni/NiO@C-2 oxidation, see the Materials and Methods for details). From Figure 5a and b, these polarization curves reveal that the onset overpotential of these Ni/NiO@C catalysts is close to that of Pt/C catalyst, implying superior HER catalytic performance at the very beginning. Furthermore, the overpotentials at a current density of 10 mA cm^{-2} for the Ni/NiO@C-2 catalyst are as low as 64 and 76 mV in 1 M KOH and 1 M PBS, respectively (Figure 5c and d), which are very impressive and comparable with that of the state-of-the-art non-precious metal catalysts (Tables S3 and S4). The optimized catalytic activities of the Ni/NiO@C-2 catalyst are ascribed to appropriate Ni/NiO ratio, which is further demonstrated by the poor catalytic activities of the Ni/NiO@C-2 oxidation with excessive NiO content. Moreover, to estimate the reaction kinetics and the rate-determining steps (RDSs) of these electrode materials, the Tafel slopes of these samples were further analyzed (Figure 5e and f). Clearly, the Ni/NiO@C-2 displays the smallest Tafel slope (55 mV dec^{-1} in 1 M KOH and 53 mV dec^{-1} in 1 M PBS) among these Ni-based catalysts, suggesting the fastest reaction kinetics. Notably, the Tafel slope of all catalysts is more than 30 mV dec^{-1}, revealing that the Volmer step (water dissociation) is RDS. Additionally, the double-layer capacitance (C_{dl}) of Ni/NiO@C-2 is significantly smaller than that of the Ni/NiO@C-2 acid treatment (Figures S15–S17), which is ascribed to porous structure due to Ni removing (Figure S18). As reported by Bao and co-workers [54], the interfacial electron penetration from the metal Ni to the graphene surface in the Ni@C structure could efficiently promote the HER in acid media. However, poor catalytic activities of the Ni/NiO@C-2 acid treatment without exposed Ni/NiO interfaces indicated that the interfacial charge

Please cite this article in press as: H. Jiang et al., (2018), https://doi.org/10.1016/j.mattod.2018.01.033

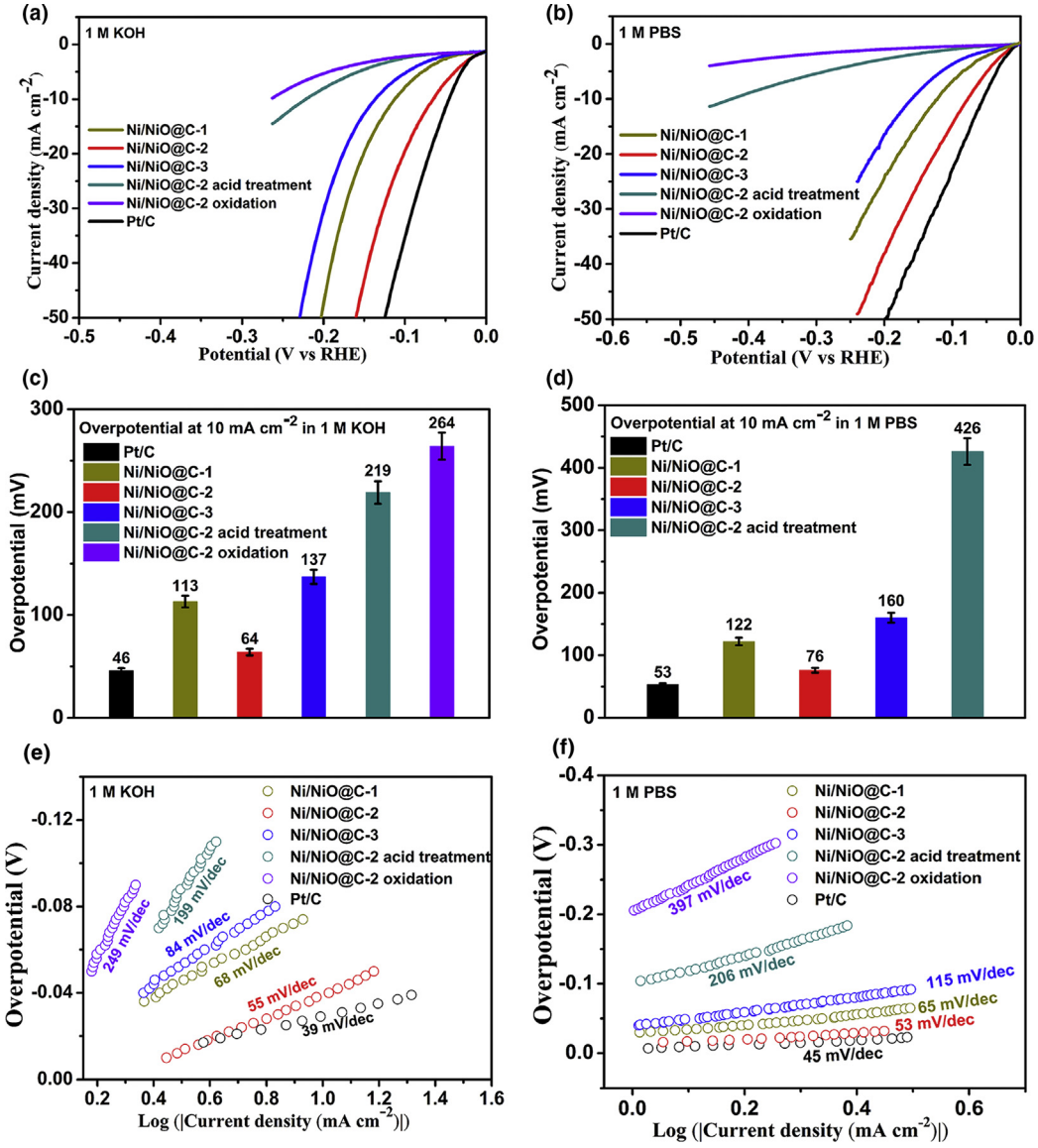

FIGURE 5

HER performance of ternary interfacial structures of the Ni/NiO@C and control samples. (a, c and e) HER performance in 1 M KOH: LSV polarization curves (a), overpotentials at a constant current density of 10 mA cm^{-2} (c), and Corresponding Tafel plots (e). (b, d and f) HER performance in 1 M PBS: LSV polarization curves (b), overpotentials at a constant current density of 10 mA cm^{-2} (d), and corresponding Tafel plots (f).

penetration is not the key in alkaline and neutral media. The high catalytic performance of the Ni/NiO@C-2 catalysts mainly stems from the accessible interface structures. Moreover, compared to previously reported metal/oxides interfacial structures [28–31], the better catalytic performance of ternary interfacial superstructures indicates that the high-density interfacial structures and metal/oxide ratios played crucial roles. The high-density interfacial structure possesses abundant metal/oxide active sites for HER. Suitable metal/oxide ratios optimized the catalytic activities. Furthermore, the accessible 3D carbon network around these Ni species with intimate contact could act as electron acceptors to facilitate the catalytic process, enabling accelerated reaction kinetics. To investigate the electrical behavior of the Ni/NiO@C-2 [45], the temperature-dependent resistivity measurement (Figure S19) reveals that the electrical resistivity of the Ni/NiO@C-2 increased with the increasing temperature, displaying typical metallic character with low resistivity at a given temperature. The metallic character facilitates electron transfer. The durability tests were also conducted using chronopotentiometry method at a constant current density of 10 mA cm^{-2} (Figure S20). The excellent long-term durability of the Ni/NiO@C-2 catalyst made it a potential candidate for practical applications. Moreover, the XRD patterns and Ni K-edge XAFS $k^3(\chi(k))$ oscillation curves of the Ni/NiO@C-2 catalyst after HER test demonstrate the maintainment of the long-range and local structure during the HER process (Figures S21 and S22). For the practical application, the Ni/NiO@C-2 catalyst was also loaded onto the carbon fiber paper with a mass loading 3 mg cm^{-2}, and also exhibits high activity and long-term stability (Figure S23).

Please cite this article in press as: H. Jiang et al., (2018), https://doi.org/10.1016/j.mattod.2018.01.033

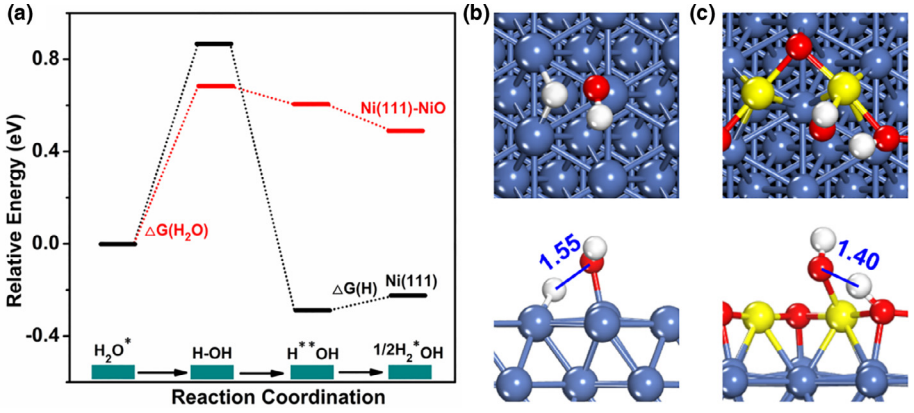

FIGURE 6

(a) HER reaction pathway of on the Ni(1 1 1) surface and Ni(1 1 1)NiO interface interfaces. $\Delta G(H_2O)$ and $\Delta G(H)$ are related kinetics energy barriers of Volmer and Tafel steps. Optimized TSs for water dissociation on: (b) Ni(1 1 1), (c) Ni(1 1 1)NiO interface. Color codes: Light blue and yellow represent Ni atoms in metal Ni and NiO, respectively. Red and white represent O and H atoms. The OH bond length (Å) at the TS is indicated.

Theoretical exploration of the interfacial effects

Considering that the water dissociation has been previously demonstrated to be identified as the RDS in the alkaline and neutral media [18–22], we employed DFT calculations to further understand the promotional effects of the Ni–NiO interface on the water dissociation. The Ni and NiO models were first constructed, where the cubic lattice parameters and the magnetic moments were in good agreement of the previous experimental and theoretical results (See Figure S24, Tables S5 and S6 for details). Then, we further modeled the Ni(1 1 1) and NiO(1 0 0) surfaces that have been observed in the HRTEM images. For the Ni—NiO interface, a chain of NiO nanoparticles was deposited on the Ni(1 1 1) surface, similar to previously reported models for oxide/Cu systems [55,56]. The atomic configurations of water dissociation step at the bare Ni(1 1 1) surface, NiO(1 0 0), and Ni (1 1 1)—NiO interface are shown in Figures S25–27, and the corresponding potential energy for HER on them are plotted (Figures 6a and S27). It is noted that on the NiO(1 0 0) surface, the water dissociation is strongly endothermic, and the free energy of hydrogen adsorption(ΔG(H)) is as high as 0.44 eV (Figure S27). This means that the bare NiO catalyst is catalytically inactive for HER, which is consistent with poor catalytic performance of the Ni/NiO@C-2 oxidation with 79.9 wt% NiO content. For the bare Ni(1 1 1) surface and the Ni(1 1 1)—NiO interface (Figures S25 and 26), water adsorbs on the atop sites of the surface Ni atoms. The Gibbs free energy of the water dissociation step (ΔG (H_2O)) for water dissociation on the Ni—NiO interface is found to be 0.68 eV, which is lower than that on bare Ni(1 1 1) surface (0.87 eV). Additionally, both the values of the free energy of hydrogen adsorption (ΔG(H)) at the bare Ni(1 1 1) surface and Ni(1 1 1)—NiO interface are very small (Table S7), further implying that the water dissociation is the RDS for the HER. The decreased energy barrier of RDS at the Ni—NiO interface is mainly due to the formation of a more favorable transition state (TS) compared to the bare Ni(1 1 1) surfaces [57]. As shown in Figure 6b and c, on the bare Ni(1 1 1) surface, the O—H bond of the H_2O needs to be stretched to 1.55 Å from 0.98 Å at the adsorbed states. For the TS on the Ni-NiO interface, the O—H bond is stretched to 1.40 Å, which is less than that on the Ni(1 1 1) surfaces with a lower energy cost for O—H bond breaking. Therefore, it can be inferred that the Ni—NiO interface decreases the energy barrier by the formation of a more favorable TS and thus facilitates the formation of absorbed hydrogen on the interface sites through water dissociation in alkaline and neutral media, thereby leading to the fast reaction kinetics. These carbon layers around the metal/oxide interfaces enable fast electron transfer to facilitate the water dissociation.

Conclusion

In conclusion, we have realized highly efficient hydrogen evolution electrocatalysis in alkaline and neutral media by unique ternary interfacial superstructure. The features of the unique ternary interfacial superstructure include that (i) the interconnected carbon layers protect the excessive oxidation of Ni nanoparticles so that stable interfacial structures could be obtained; (ii) the abundant metal/oxide interfaces could act as highly active sites for water dissociation; and (iii) these carbon layers around the metal/oxide form three dimensional conduction network to enable fast electron transfer. Furthermore, this work has presented an excellent demonstration to shed light on the interfacial properties and consequent effects toward efficient electrocatalysts via synchrotron radiation-based X-ray spectroscopic characterizations and DFT calculations.

Materials and methods

Synthesis of the Ni/NiO@C and control samples

EDTA–Ni was prepared according to previous reports with some modifications [58]. First, A solution: H_4EDTA (3.54 g, 10.0 mmol) and triethylamine (10.0 mL, 72.0 mmol) were dissolved 150 mL of N,N-dimethylformamide (DMF) and stirred at 50 °C to obtain uniform solution. B solution: $Ni(NO_3)_2$ $6H_2O$ (5.80 g, 20.0 mmol) was added to 100 mL of DMF and stirred to achieve the dissolution of Ni salts. Then, B solution was added to A solution under sustainable magnetic stirring. Finally, the resulting solid was washed with neat DMF, and was collected after drying in 100 °C. Yield: 5.74 g, 94.9%. The synthesis of the EDTA–Ni is facile and can be large-scale production. For the synthesis of

Please cite this article in press as: H. Jiang et al., (2018), https://doi.org/10.1016/j.mattod.2018.01.033

the Ni/NiO@C, the as-prepared EDTA–Ni (5.74 g) was grounded to powder and heated to designed temperature (400 and 500 °C) with a heating rate of 5 °C min^{-1} under an Ar flow rate of 500 mL min^{-1} for 180 min. Then, the two annealed fresh samples were deposited in the air for one month so that the relatively stable ternary structures (1.71 g, Yield: 29.8%), the Ni/NiO@C-1 and Ni/NiO@C-2, were obtained. For comparison, the Ni/NiO@C-3 was obtained by depositing the 500 °C-annealed fresh sample into the Ar-protected glove box at room temperature. In addition, the Ni/NiO@C-2 encountered 1 M HCl acid etching at room temperature for 8 h to the Ni/NiO@C-2 acid treatment. Moreover, the control sample, the Ni/NiO@C-2 oxidation, was obtained by oxidizing the Ni/NiO@C-2 at 250 °C for 2 h.

Materials' characterization

PXRD was carried out with a Philips X'Pert Pro Super diffractometer with Cu Kα radiation ($\lambda = 1.54$ Å). The morphology and microstructures were observed by a JEM-2100F field emission TEM with an acceleration voltage of 200 kV. The EDX elemental mapping characterizations were also taken with JEM-2100F field emission transmission. The TGA data were obtained in TGA/DSC (TGA Q5000) instrument with a heating rate of 10 °C min^{-1} at air. X-ray photoelectron spectroscopy (XPS) measurements were undertaken at the Catalysis and Surface Science End Station at the BL11U beamline of National Synchrotron Radiation Laboratory (NSRL) in Hefei, China. The binding energies were calibrated using the C 1s level at the energy of 284.5 eV as a reference. The Raman spectrum was recorded with a Bruker RFS 100/S spectrometer to analyze the carbon. The Ni L-edge and C K-edge XANES spectra were recorded in BL12B-α of the NSRL. The XAFS measurements at the Ni K-edge were performed in transmission mode at the BL14W1 of the Shanghai Synchrotron Radiation Facility (SSRF). The X-ray was monochromatized by a double-crystal Si(1 1 1) monochromator. The storage ring of SSRF was operated at 3.5 GeV with the current of 300 mA. The as-obtained XAS data were processed according to the standard procedures using the WinXAS3.1 program. Linear combination fitting (LCF) in Athena program was performed to determine the ratios of Ni and NiO components. The electrical conductivity was recorded using a Keithley 4200-SCS semiconductor characterization system by a four-point probe configure.

Electrochemical measurements

All electrochemical measurements were carried out on a conventional three-electrode system with an electrochemical workstation (CHI 760E). Ag/AgCl (saturated KCl) electrode was used as the reference electrode and a graphite rod was used as the counter electrode. 4 mg of the samples and 40 μL 5% Nafion solution were put in 1 mL mixture of water/isopropanol with a volume ratio of 3:1 and dispersed by ultrasonication for at least 60 min to form a homogeneous ink. After that, 5 μL of this ink was carefully dropped onto a glassy carbon electrode (GCE) with a diameter of 3 mm and dried in air atmosphere to form a catalyst mass loading of about 0.272 mg cm^{-2}. Also, the ink was loaded onto a carbon fiber paper, achieving a catalyst loading of 3 mg cm^{-2}. The potentials were converted to reversible hydrogen electrode (RHE) using this equation: $E_{RHE} = E_{Ag/AgCl} + 0.059\ pH + 0.197$ V. The polarization curves were recorded with a scan rate of 5 mV s^{-1} in N_2-saturated 1 M KOH and 1 M PBS (purged with pure N_2 for at least 60 min) with a 90% IR compensation. The double-layer capacitance C_{dl} was determined by taking cyclic voltammetry in the potential windows 0.024–0.222 V versus RHE under different scan rates ranging from 20 to 120 mV s^{-1}. By plotting $\Delta j = (j_a - j_c)$ at 0.123 V versus Ag/AgCl reference electrode against the scan rate.

Theoretical calculations

All periodic spin-polarized DFT calculations were carried out using the Vienna ab initio simulation package (VASP) [59–61]. The interactions between ion cores and valence electrons were performed by the projector-augmented wave (PAW) method [62], and the exchange–correlation energy of the electrons was dealt with the functional of GGA-PBE [63,64]. For the calculation of the nickel oxide catalyst, which is a correlated system, the DFT + U approach was further adopted with the use of the Hubbard term (U) of 6.3 eV [65]. The energy cutoff was set to 400 eV, and the atomic positions were allowed to relax until the energy and force were less than 10^{-5} eV and 0.03 eV/Å, respectively. The Brillouin zone sampling was performed using a Monkhorst–Pack grid [66], and electronic occupancies were determined in light of a Methfessel–Paxton scheme with an energy smearing of 0.2 eV [67]. The Dimer method [68] was used to determine the transition states of the elementary step of water dissociation. The zero-pointenergy and entropic corrections at 298.15 K were taken into account for the Gibbs free energies diagram of hydrogen evolution. The Ni(1 1 1), Ni(1 0 0), and NiO (1 0 0) surfaces were all calculated on p(3 × 3) supercell slabs with four layers and a 10-Å vacuum spacing between slabs. The Ni (1 1 1)/NiO and Ni(1 0 0)/NiO interfaces were modeled with a chain of NiO nanoparticles deposited on Ni(1 1 1) and Ni(1 0 0) surfaces, similar to previously reported model for oxide/Cu systems [55,56].

Acknowledgments

This work is financially supported by MOST (2017YFA0303500, 2014CB848900), NSFC (U1532112, 11574280, 11605201, 21706248), Innovative Research Groups of NSFC (11621063), CAS Key Research Program of Frontier Sciences (QYZDB-SSW-SLH018), China Postdoctoral Science Foundation (BH2310000033), CAS Interdisciplinary Innovation Team, Innovative Program of Development Foundation of Hefei Center for Physical Science (T6FXCX003). L. S. acknowledges the recruitment program of global experts, the CAS Hundred Talent Program, Key Laboratory of Advanced Energy Materials Chemistry (Ministry of Education) Nankai University, Key Laboratory of the Ministry of Education for Advanced Catalysis Materials and Zhejiang Key Laboratory for Reactive Chemistry on Solid Surfaces (Zhejiang Normal University). We thank the Shanghai synchrotron Radiation Facility (14W1, SSRF), the Beijing Synchrotron Radiation Facility (1W1B and soft-X-ray endstation, BSRF), the Hefei Synchrotron Radiation Facility (ARPES, Photoemission, MCD and Catalysis/Surface Science Endstations, NSRL), and the USTC Center for Micro and Nanoscale Research and Fabrication for helps in characterizations. Thank Chuanqiang Wu and Shuangming Chen for helps on TEM and XAFS tests.

Please cite this article in press as: H. Jiang et al., (2018), https://doi.org/10.1016/j.mattod.2018.01.033

Appendix A. Supplementary data

Supplementary data associated with this article can be found, in the online version, at https://doi.org/10.1016/j.mattod.2018.01.033.

References

[1] T.R. Cook et al., Chem. Rev. 110 (2010) 6474–6502.
[2] X. Zou, Y. Zhang, Chem. Soc. Rev. 44 (2015) 5148–5180.
[3] A.S. Aricò et al., Nat. Mater. 4 (2005) 366–377.
[4] K. Zeng, D. Zhang, Prog. Energy Combust. Sci. 36 (2010) 307–326.
[5] P. Chen et al., Angew. Chem. Int. Ed. 55 (2016) 2488–2492.
[6] L. Bu et al., Nat. Commun. 7 (2016) 11850.
[7] G. Zhang et al., J. Am. Chem. Soc. 138 (2016) 14686–14693.
[8] D.-Y. Wang et al., J. Am. Chem. Soc. 137 (2015) 1587–1592.
[9] H.B. Wu et al., Nat. Commun. 6 (2015) 6512.
[10] J.-X. Feng et al., Angew. Chem. Int. Ed. 56 (2017) 8120–8124.
[11] J. Yin et al., J. Am. Chem. Soc. 138 (2016) 14546–14549.
[12] Y. Zheng et al., Angew. Chem. Int. Ed. (2017), https://doi.org/10.1002/anie.201710556.
[13] T. Zhang et al., Nano Energy 43 (2018) 103–109.
[14] T. Ling et al., Nat. Commun. 8 (2017) 1509.
[15] J.L. Liu et al., Nano Energy 40 (2017) 264–273.
[16] Y. Zheng et al., J. Am. Chem. Soc. 138 (2016) 16174–16181.
[17] B. Bayatsarmadi et al., Small 13 (2017) 1700191.
[18] J. Deng et al., Energy Environ. Sci. 7 (2014) 1919–1923.
[19] H. Yin et al., Nat. Commun. 6 (2015) 6430.
[20] I. Ledezma-Yanez et al., Nat. Energy 2 (2017) 17031.
[21] R. Subbaraman et al., Science 334 (2011) 1256–1260.
[22] Z.-L. Wang et al., J. Am. Chem. Soc. 137 (2015) 15070–15073.
[23] Q. Lu et al., Nat. Commun. 6 (2015) 7567.
[24] M.S. Faber, S. Jin, Energy Environ. Sci. 7 (2014) 3519–3542.
[25] C.C.L. McCrory et al., J. Am. Chem. Soc. 137 (2015) 4347–4357.
[26] H.I. Karunadasa et al., Science 335 (2012) 698–702.
[27] B. Zhang et al., Science 352 (2016) 333–337.
[28] N. Danilovic et al., Angew. Chem. Int. Ed. 54 (2012) 2100–2104.
[29] J.X. Feng et al., Angew. Chem. Int. Ed. 56 (2017) 2960–2964.
[30] M. Gong et al., Angew. Chem. Int. Ed. 54 (2015) (1993) 11989.
[31] Y. Kuang et al., Angew. Chem. Int. Ed. 55 (2016) 693–697.
[32] R. Toh et al., Chem. Asian J. 8 (2013) 1295–1300.
[33] Z. Sofer et al., ACS Nano 8 (2014) 7106–7114.
[34] X. Chia et al., Chem. Eur. J. 20 (2014) 17426–17432.
[35] Y. Chen et al., Angew. Chem. Int. Ed. 56 (2017) 6937–6941.
[36] W. Liu et al., Chem. Sci. 7 (2016) 5758–5764.
[37] W. Sheng et al., Energy Environ. Sci. 10 (2017) 1180–1185.
[38] B. Qiao et al., Nat. Chem. 3 (2011) 634–641.
[39] P. Liu et al., Science 352 (2016) 797–800.
[40] Q. Liu et al., Adv. Mater. 27 (2015) 4837–4844.
[41] S. Chen et al., Nano Lett. 15 (2015) 5961–5968.
[42] F. Lei et al., Nat. Commun. 7 (2016) 12697.
[43] T. Ling et al., Nat. Commun. 7 (2016) 12876.
[44] Q. Liu et al., ACS Nano 11 (2017) 6483–6491.
[45] H. Liu et al., ACS Nano 11 (2017) 11574–11583.
[46] M. Gong et al., Nat. Commun. 5 (2014) 4695.
[47] R.J.O. Mossanek et al., J. Phys.: Condens. Matter 25 (2013) 495506.
[48] S. Uhlenbrock et al., J. Phys.: Condens. Matter 4 (1992) 7973.
[49] J. Jiang et al., Nano Energy 38 (2017) 175–184.
[50] W. Che et al., J. Am. Chem. Soc. 139 (2017) 3021–3026.
[51] Y. Liang et al., Nat. Mater. 10 (2011) 780.
[52] K. Feng et al., Angew. Chem. Int. Ed. 55 (2016) (1954) 11950–11951.
[53] Y. Zhao et al., Angew. Chem. Int. Ed. 55 (2016) 4215–4219.
[54] J. Deng et al., Angew. Chem. Int. Ed. 54 (2015) 2100–2104.
[55] P. Liu, J. Chem. Phys. 133 (2010) 204705.
[56] L.-Y. Gan, Y.-J. Zhao, J. Phys. Chem. C 116 (2012) 16089–16092.
[57] H. Wang et al., J. Am. Chem. Soc. 135 (2013) 4149–4158.
[58] K.J. Lee et al., Chem. Commun. 51 (2015) 6773–6776.
[59] G. Kresse, J. Furthmüller, Phys. Rev. B 54 (1996) 11169–11186.
[60] G. Kresse, J. Hafner, Phys. Rev. B 47 (1993) 558–561.
[61] G. Kresse, J. Hafner, Phys. Rev. B 49 (1994) 14251–14269.
[62] P.E. Blöchl, Phys. Rev. B 50 (1994) 17953.
[63] G. Kresse, D. Joubert, Phys. Rev. B 59 (1999) 1758–1775.
[64] J.P. Perdew, K. Burke, M. Ernzerhof, Phys. Rev. Lett. 77 (1996) 3865–3868.
[65] M. Gajdoš, J. Hafner, Surf. Sci. 590 (2005) 117–126.
[66] H.J. Monkhorst, J.D. Pack, Phys. Rev. B 13 (1976) 5188–5192.
[67] M. Methfessel, A.T. Paxton, Phys. Rev. B 40 (1989) 3616–3621.
[68] G. Henkelman, H. Jónsson, J. Chem. Phys. 111 (1999) 7010–7022.

Please cite this article in press as: H. Jiang et al., (2018), https://doi.org/10.1016/j.mattod.2018.01.033